MARS Spectral CT: Image quality performance parameters using the Medipix3.0 detector

---

A thesis submitted in partial fulfilment of the
requirements for the Master of Science in Medical Physics
at the University of Canterbury

by

Nate Dikai Tang

Department of Physics and Astronomy
University of Canterbury

March 5, 2013

Abstract

The research in this thesis was undertaken because information on the relationship between scan parameters and image quality for the MARS spectral CT was lacking. However, the MARS spectral CT is expected to extend into clinical use in the future, so it is absolutely crucial that we know how the quality of the images that it produces is effected by different scan parameters. This will allow us to make further improvements to the machine, and ultimately help clinicians to visualise important information in patients which are not revealed by other imaging modalities.

This thesis provides information on how the image quality is affected by different scan parameters on the MARS spectral CT using a Medipix3 silicon quad detector. In particular, it explores how different numbers of projections, exposure time products (mAs), and peak tube voltages (kVp) with different threshold energies (kV) effect the image noise, image resolution and image uniformity, respectively. This provides a set of guidelines for future work using the MARS scanner to obtain images of optimal quality. This thesis also determines that the new image reconstruction software mART developed by Niels de Ruiter, is a suitable replacement for the reconstruction software OctopusCT that is currently being used by the MARS team. Using mART reduces the scan times and dose delivered by the MARS spectral CT.

Acknowledgements

I would like to thank my supervisors Professor Phil Butler, Dr Anthony Butler, Dr Judy Mohr and also Steven Bell from the MARS team, for all the assistance and guidance on my thesis that they provided me with through regular meetings. Also I would like to thank Alexander Chernoglazov from HITLab NZ, for using his computer software to visualise my 2D mouse scan-data into a 3D mouse model, which is presented at the end of Chapter 5.

The Python codes written by Dr Judy Mohr saved me time by allowing me to emulate scan-data from a full data set rather than having to do multiple scans to acquire the individual data sets. The emulation performed by the Python codes also ensured that each of my emulated datasets were consistent with each other, increasing the experimental accuracy. The Matlab codes written by Edward Linscott, a 2012 summer research student from the MARS team before I started my thesis, allowed me to use them as a solid template from which I was able to make further minor modifications to, in order to carry out my image quality analysis on the reconstructed images in Chapter 5. In addition, I was able to receive help from Alexander Chernoglazov from the NZ HITLAB, where he used his 3D visualisation software to reconstruct my 2D mouse images into a full 3D model. Lastly, I would like to acknowledge Niels de Ruiter for his creation of the new reconstruction software mART, for which I performed image quality analysis of it against the currently used reconstruction software OctopusCT. In addition, I coordinated efforts on writing this work into a scientific publication where I also wrote as the lead author, which was later presented at the Imaging and Vision Computing New Zealand Conference 2012, and discussed in Chapter 6.

Contents

List of Figures

Chapter 1

Introduction

Spectral Computed Tomography (CT) promises to be a major advance of current grey scale CT. The use of energy (or colour) information can provide a new ability to differentiate different types of tissues. Imaging plays a critical role in visualising the anatomy of patients in hospitals. From the discovery of x-rays by Roentgen in 1895, "plain-film" x-ray images often known simply as an x-ray, have been the mainstay of imaging. The invention of x-ray CT in 1972 has been considered the greatest innovation in imaging since plain film x-rays. CT now plays an irreplaceable role in diagnostic radiology. It is the most common imaging modality in hospitals and the quality of CT images is steadily improving and the use of CT is still growing rapidly. However, neither conventional plain-film x-rays, nor can CT accurately differentiate different types of tissues.

In recent years both Siemens and GE have introduced two-energy CT systems, which are called "Dual-energy CT™" and "Spectral CT™", respectively. Two-energy CT is an improved version of the conventional CT and gives more information about the patients' anatomy. Two-energy CT exposes the patient to x-rays from two energy spectrums which in turn enables better tissue differentiation and ligament/tendon visualisation. CT is today's main structural imaging modality. Positron emission tomography (PET), and single-proton emission computed tomography (SPECT) are functional imaging modalities. Both are performed by the injection of a

gamma-ray-emitting radioisotope into the blood. Another imaging modality that can be found in hospitals is the Magnetic Resonance Imaging (MRI), which uses the interaction of magnetic fields and protons in the body to produce images. MRI is both a structural and functional imaging modality. All these modalities, can with the help of contrast agents, identify anatomical abnormalities and provide basic information about the location, size and spread of tumours. However, these contrast agents are not target specific, and cannot reliably detect tumours that are smaller than 0.5 cm. In addition, standard CT and MRI barely distinguish between benign and cancerous tumours [*Rusinek H*(1998)]. Consequently, there is a need for a new imaging modality. Spectral CT is an emerging candidate.

Spectral CT is being developed by the Medipix All Resolution System (MARS) team from the University of Canterbury for pre-clinical scanning using Medipix3. In addition to measuring the structural information like other CT imaging modalities do, it also measures the molecular information and in particular, the composition of materials. The MARS spectral CT is mainly involved in differentiating different types of tissues and molecular imaging. It promises to be more useful than other imaging modalities, because it allows the use of a single broad energy spectrum x-ray beam, which is registered on an energy selective detector that measures the full attenuation spectra of the x-ray beam. This extra data enables better tissue characterisation, differentiation and contrast than the other imaging modalities. In this thesis, colour is added to the images based on the information obtained from the multi-energy spectral x-ray beam. The pre-clinical work of the MARS teams mainly involves the scanning of small animal samples, such as mice and rats, and excised human tissues such as atheromas. The MARS team is also focussing on the use of spectral CT for molecular imaging at a histological scale, which is anticipated to overcome the relatively low inherent contrast between soft tissues. Molecular imaging works by distinguishing the high attenuation of elements such as calcium from gold/iodine nanoparticles

that act as contrast agents and are as small as fractions of a micron in size. Therefore it is important to know the optimal scan parameters which will produce images that reveal as much detail as possible, and this will be the focus of this thesis, where the relationship between different scan parameters and image quality will be investigated using the MARS spectral CT.

1.1 Thesis Organization

This thesis is organised as follows:

Chapter 2 will provide a background of x-ray CT and review a list of the current imaging modalities in hospitals.

In Chapter 3, spectral CT will be discussed as well as its association with molecular imaging using gold nanoparticles. In addition, the Medipix3 chip used by the MARS spectral CT will be looked in more detail.

Chapter 4 discusses the dependent variables in the analysis of image quality, which are composed of: image noise, image resolution and image uniformity.

Chapter 5 shows the results of how the dependent variables are affected by the scan parameters which are composed of: number of projections, exposure time product, and peak tube voltages with different threshold energies. The results are analysed and discussed.

Chapter 6 presents the new image reconstruction software called mART and compares it to OctopusCT.

1.2 Publication

The work presented in Chapter 6 was collaborative and published in the Imaging and Vision Computing New Zealand Conference in November 2012. It details the preliminary work completed before a spectral reconstruction algorithm may be developed. A small reconstruction software called mART was created by Niels de Ruiter which implements a Simultaneous Algebraic

Reconstruction Technique (SART). I thoroughly compared the reconstructed images from mART with those from OctopusCT, which is the current reconstruction software used by the MARS team, in order to determine the suitability of replacing OctopusCT with mART.

Chapter 2

Computed Tomography

This chapter will review how greyscale x-ray CT works. It will also introduce spectral CT and its implementation by the Medipix3 detector.

2.1 Generation of x-rays

X-rays are a form of electromagnetic radiation and was discovered by Wilhelm Roentgen[*Sie*(2011)], who had named it as such to emphasise an unknown type of radiation.

In the MARS spectral CT, x-rays are generated by an x-ray tube. This is a vacuum tube that accelerates the electrons that have been excited from a hot cathode to high velocities with a high voltage. These electrons hit the metallic anode (high-atomic number element, in our case tungsten) inside the tube, from which x-rays are produced by two main processes: Bremsstrahlung and characteristic radiation. Bremsstrahlung radiation is produced when the high velocity electrons are scattered by the strong electric fields surrounding the tungsten nuclei of the anode. Characteristic radiation is produced when the remaining electrons with enough kinetic energy knock out orbital electrons from the lower energy shells of the anode atom, causing the electrons from higher energy shells to fill up the vacancy, simultaneously releasing x-ray photons[*Serman*(2011)]. Therefore, it is important to note that the spectrum from the x-ray tube contains x-rays with both discrete(characteristic radiation) and continuous(Bremsstrahlung) energy levels. For this project, x-ray

tube energies in the range of 30 peak kilo-volt (kVp) to 50kVp were used because 50kVp is the maximum tube voltage that can be safely tolerated without damage by the Medipix3.0 silicon quad chip used for the experiments, and any voltages below 30kVp do not produce sufficient photons to reach the detector.

2.2 Absorption/Attenuation Coefficients of Materials

The intensity of x-rays decrease exponentially when they pass through a matter of thickness x. This phenomenon is formulated by the Beer-Lambert Law

$$I = I_0.e^{-\mu} \tag{2-1}$$

where I_0 is the incident intensity of the x-ray beam and μ is the linear attenuation coefficient of the material. Each material has its own attenuation curve, and is illustrated in Figure 2.1 for a representative list of elements. For x-rays of energies below 1MeV, the decrease of intensity when interacting with matter is caused by two main processes: the photoelectric effect and Compton effect. The exact energy of the x-ray and the mass absorption characteristics of the target (which directly relates to the atomic number, Z) will determine which process dominates, and this is schematically shown in Figure 2.2

The photoelectric effect occurs when a photon interacts with an atom whose K-shell electron binding energy is just below the kinetic energy of the photon. This results in a sudden increase in the attenuation coefficients of the photons with that energy, illustrated by the zigzag pattern of the trends in Figure 2.1 and triggers the ejection of electrons from the K-shell of the atom due to the atomic instability caused by the extra energy imparted from the photons. Therefore, the photoelectric effect leaves the atom in an ionised state. This forces the electrons from an outer shell to fill in the vacancy, emit-

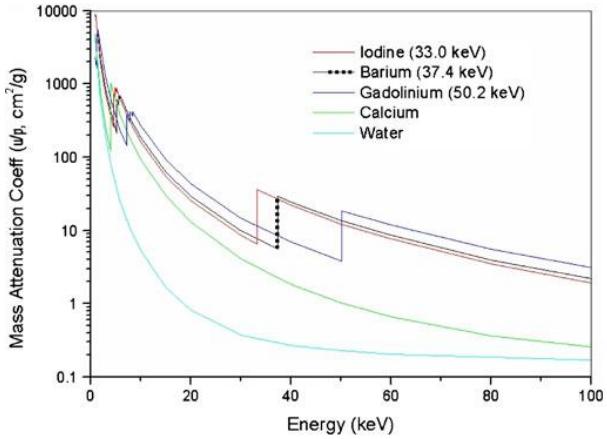

Figure 2.1: The individual attenuation curves for different elements, reprinted from [*N. G. Anderson*(2010)].

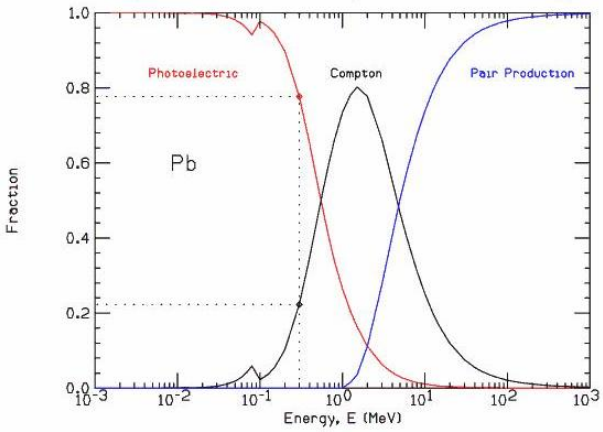

Figure 2.2: This diagram shows the relative contribution from each of the photoelectric, Compton and pair production processes towards the interaction of x-rays with matter as a function of energy, represented by the three different curves, reprinted from [*Nelson*(2001)].

ting a characteristic x-ray in the process and stabilising the atom. The photoelectric effect dominates at energies up to 500keV[*Connolly*(2012)]. This is especially so in atoms with high atomic numbers. When contrast agents consisting of heavy elements like gadolinium, gold or bismuth are used, their K-shells become accessible for diagnostic x-ray imaging. By making multiple spectrally distinct measurements using multi-bin energy-discriminating counting detectors, these K-edge features can be discriminated from other contributions to the x-ray attenuation[*E and R*(2007)]. This technique is referred to as spectral CT, and will be explained in detail in Chapter 3.

The Compton effect (incoherent scattering) is observed when an x-ray photon hits and transfers a part of its kinetic energy to the electron of an atom. The photon loses part of its energy and changes direction while its momentum is conserved. Therefore an increase in wavelength (decrease in energy) is observed in this scattered photon. The Compton effect dominates at energies of 100keV to 10MeV[*Connolly*(2012)], and especially so in atoms with low atomic numbers.

An additional process that exists in the interaction of x-rays with matter is pair production. When an x-ray photon with sufficient energy interacts with an atomic nucleus, a pair of electron and positron is created. However, this process only occurs for x-rays of energies in excess of 1.02MeV[*Connolly*(2012)], which is higher than those used by the MARS spectral CT, and so it will not be discussed any further in this thesis.

2.3 Modern Imaging Modalities

A typical hospital CT uses x-rays that consist of photons from a range of energies. The photons are attenuated to different degrees depending on the tissues they penetrate. An image obtained from a CT scan which involves rapidly rotating the x-ray tube and shooting x-ray beams over 360 degrees around a patient, shows non-superimposed and cross-sectional areas of the body. The x-ray photons transmitted through the attenuating patient is reg-

istered on a ring of detectors located around the patient, and with the help of a computer, a final image is reconstructed from all the x-ray beams. However, even though a CT image possesses better contrast, and allows better visualisation of various differently structured regions of soft-tissues than a conventional x-ray image does, it does not fully differentiate between different types of soft tissues. This is because, it is the sum of the total attenuation across all the tissues over the whole photon energy spectra that is registered on the detector, and not the separate attenuations across individual tissues. This results in the output of an image that has only a one-dimensional attenuation value in its energy domain.

Apart from CT, another renowned medical imaging modality is the Magnetic Resonance Imaging (MRI). However, MRI has shortcomings on its own: MRI cannot be used on patients who have received implants such as surgical clips, metallic fragments, cardiac monitors and pacemakers. The time taken for a scan inside the MRI machine is also very long, ranging from 20 to 45 minutes, which is unsuitable for use in emergency rooms and on claustrophobic patients, especially with the constant noise that the machine makes. Another disadvantage associated with a MRI scan is its expensive cost, which is usually double or triple that of a CT scan.

Single-photon emission computed tomography (SPECT) is a nuclear medicine tomographic imaging technique that uses radioactive tracers. Before a SPECT scan, the patient is injected with a chemical containing tracers that are radiolabelled, which emit gamma rays that are registered on the scanner's detector. A computer then collects this information and generates 3D information, which is typically presented as cross-sectional slices through the patient. However, as well as having a very poor spatial resolution of just 1 mm, the SPECT images are limited to showing only areas where the blood flows, as the tracers remain within the blood stream instead of being absorbed into the surrounding tissues. Because a high spatial resolution is needed for the MARS team's pre-clinical work involving the imaging of nanoparticles and

small biological samples i.e. atherosclerotic plaques, a resolution of 1 mm will not suffice.

The Siemens "Dual-energy CT™" is also a diagnostic imaging technique which uses two different x-ray tubes in a single CT unit. It allows the patient to be exposed to x-rays from two different energy spectrums, allowing enhancements in the image contrast, tissue differentiation and ligament/tendon visualisation. The two different x-ray tubes in the two-energy CT are used to acquire both high and low voltage images. Because the voltage across the tube determines the energy and hence the attenuation of the x-ray beam which in turn defines the image, each image acquired is energy dependent.

The GE "Spectral CT™" switches the accelerating voltage rapidly between high and low values. By measuring the attenuation of the two x-ray beams over the two energies, and knowing of the material dependency of the energies of the x-ray beams, the two-energy CT makes it possible to form assumptions about the properties of the attenuating material by analysing the spectral properties of the detected beam[*Riedel*(2011)]. Two-energy CT is particularly useful in angiography. Based on the spectral properties of different body parts, the bones can be identified with the use of two-energy CT and then removed from the angiogram, leaving iodine as the only dense material in the blood vessel. This allows the iodine inside the blood vessel lumen to be imaged with superb quality, near that of magnetic resonance angiography, and provide an accurate estimation of abnormalities such as arterial stenoses. Two-energy CT has established itself well as a tool for radiological diagnosis in hospitals; however, its exposure of two overlapping sources of x-ray spectra poses disadvantages such as increased image noise and x-ray dosage. In addition, despite the ability of a two-energy CT to discriminate two tissues possessing very different attenuation profiles, it does not accommodate for the similarity between the very many different tissues in the human body[*Anderson et al.*(2010)]. This greatly limits the reliability of an image whose data was obtained from two different tissue types with

very closely lying attenuation profiles on the spectral curve. This motivates the development of spectral CT, as it promises to eliminate these problems and introduce many new benefits.

Chapter 3

Spectral CT

Spectral CT utilises the different energy-specific attenuation profiles (different linear attenuation coefficients due to the different atomic structure of tissues) of the different types of tissues in the body that the x-ray passes through. An energy discriminating detector differentiates the attenuation spectra of the x-ray beam, and provides images of more detailed tissue characterisation, differentiation and contrast than those of conventional CT. This way, even if different tissues were to have very similar attenuation values, they can still be accurately differentiated from each other[*Anderson et al.*(2010)]. Colour can also be added to the image using information that has been obtained from the x-ray energy spectra, without the loss of any spatial resolution. Beam hardening artifacts are also reduced in this new technology. Chapter 4 explains that beam hardening, a consequence of the variation of absorption with photon energy, is in fact our signal, not an artifact to be removed.

One important use of spectral CT is for the imaging of vascular atheroma plaques. Because the energy dependence of the attenuation coefficients of both calcium and iron are unique, were they to appear in a same image, they would be easily identified and differentiated if sufficiently accurate spectral measurements were taken. If we can differentiate iron from calcium in the plaques, then this would give information about the characteristics of the plaques to help clinicians identify those plaques that are most likely to rup-

ture and cause a stroke or heart attack.

The Medipix3 chip is discussed in section 3.1 below. Medipix3 detectors distinguish both the density and atomic structure of a sample. The brightness of the image is determined by the sample's density, and the colour of the image is determined by the sample's atomic structure[*R. Ballabriga*(2010)].

Molecular imaging is a novel imaging technique that integrates molecular biology with in vivo imaging. This helps to obtain information about biological processes and to identify diseases based on molecular markers such as gold nanoparticles because gold induces a strong x-ray attenuation. The gold nanoparticle also has unique physical, chemical and biological properties, which make it an ideal candidate for molecular imaging [*Al-Nahhas A*(2007), *Nanni C*(2006)]. Different tissues have different atomic numbers and electron densities and thus provide different degrees of x-ray attenuation, where a higher attenuation allows for better soft tissue differentiation[*Connor EE*(2005)]. The atomic number and electron density of gold (79 and $19.32\,g/cm^3$, respectively) are much higher than those of the currently used CT contrast agents such as iodine (53 and $4.9\,g/cm^3$), which means that gold has a distinctive energy dependence in its attenuation coefficient. Therefore, by using gold nanoparticles for molecular imaging with the MARS spectral CT, the ability to distinguish between different tissues will be enhanced, which is what makes it superior to standard CT and MRI. In addition, unlike iodine, a gold nanoparticle is nontoxic and its versatile surface chemistry allows it to be coated with a variety of biological recognition molecules[*Hauck TS*(2008)].

3.1 Overview of the MARS Medipix Chip

The detector used for the x-ray detection in this project was the silicon quad Medipix 3 detector. This is a photon counting pixel detector that was developed by an international collaboration hosted by the European Organisation for Nuclear Research[*R. Ballabriga*(2010)].

The Medipix3 detector consists of a complementary metal-oxide-semiconductor (CMOS) pixel detector readout chip that bonds to a semiconductor sensor. The sensor is made of either silicon, gallium arsenide (GaAs) or cadmium telluride (CdTe)[*R. Ballabriga*(2010)]. Silicon was used for this project due to its wide availability in good quality. Just like how a camera operates, the amount of information that it receives depends on the number of particles that hit the detector pixels when the electronic shutter is open.

Medipix3 is an energy selective, photon-processing pixel detector. It makes colour imaging and running no-dead time operation possible. The dimension of the detector is 256×256 pixels, and the area each pixel occupies is $0.055\,\text{mm} \times 0.055\,\text{mm}$, giving a total area of $14.08\,\text{mm} \times 14.08\,\text{mm}$[*R. Ballabriga*(2010)].

When an x-ray photon arrives at the semiconductor sensor inside the Medipix3 detector, the photoelectric effect creates an electron/hole cloud. This cloud of charge then drifts under the influence of the electric field and through the bump bonds where it is processed by the CMOS layer which counts it as a photon arrival event in the detector pixel. With the use of an energy window, only the photons within a specified energy range that arrive at the detector pixels are counted by the CMOS layer as photon arrival events. The energy window is specified by a low energy threshold (THL) that is typically set at 15 kilo-volt (kV) to allow a broad spectrum of data to be collected from photons with energies upwards of 15kV. This makes full spectroscopic x-ray imaging possible[*CERN*(2012)].

The Medipix3 detector is expected to achieve greater energy resolution than conventional detectors due to the mitigation of the charge sharing effect. This is achieved by the real-time charge summation between neighbouring pixels and the allocation of that sum to the single pixel that has the highest collected charge[*CERN*(2012)]. Figure 3.1 shows a schematic diagram of the Medipix3 chip, where a magnified cut-away view of all its different layers can be seen.

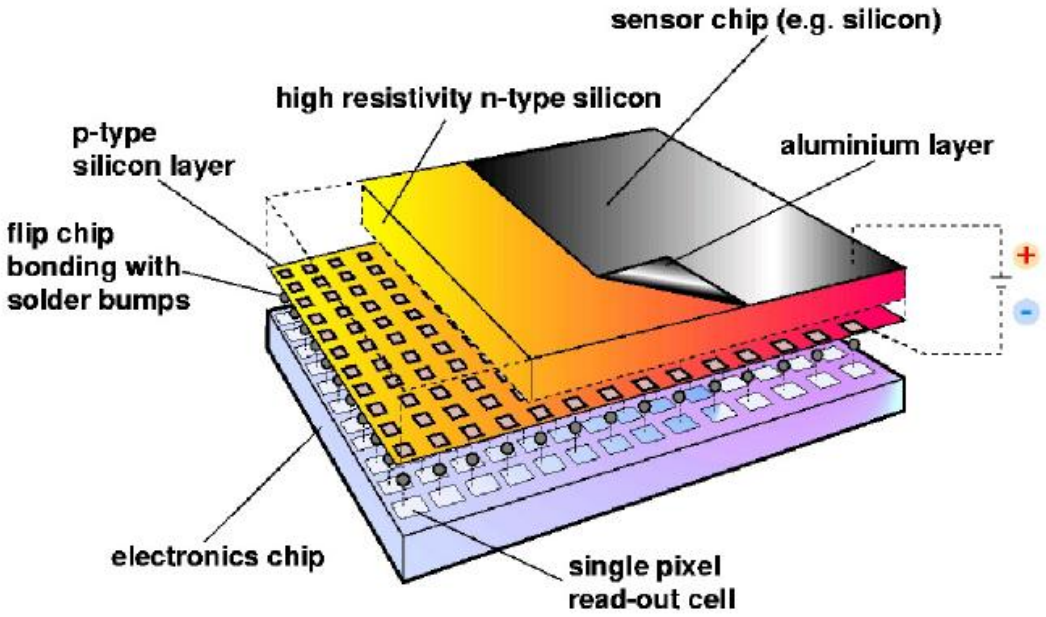

Figure 3.1: Schematic diagram of the Medipix3 chip, reprinted from [*CERN*(2012)].

3.2 Limitations

Medipix 3.0 was the first and only version from the Medipix3 detector family that was available at the time of this project. It had problems associated with equalisation instability, where the newly calibrated detector would not hold its equalisation for more than a couple hours. This introduced a degree of inconsistency into the experimental data because most of the scans took at least one hour to complete, which would have given the equalisation instability a chance to affect the images. As a result, noise was very high in the images obtained from the scans using Medipix 3.0.

Shortly after the main bulk of my experiments were completed, the newer detector version Medipix 3.1 became available and fixed the problems related to equalisation instability. The equalisation of Medipix3.1 would hold for a good several weeks rather than a couple hours, allowing a decent number of runs and a decent number of quality information to be obtained before it had to be re-equalised. As a consequence, the MARS team was able to start work on spectroscopic scanning. However, due to the fact that 1 out of the 8 counters in this detector was faulty, the images were still filled with a noticeable amount of noise, and even more so when the detector went into full spectroscopic mode.

The latest detector version Medipix 3.2 addressed all of these problems, and had a properly working charge summoning mode, something that never worked in either Medipix 3.0 or Medipix3.1. Unfortunately, Medipix3.2 was not available for pre-clinical scanning at the time that my experiments were undertaken.

Chapter 4

Parameters of Image Quality

The assessment of image quality is an important part of diagnostic radiology. It measures the image degradation in relation to that of an ideal image, which is caused by the various distortions and artifacts from within the imaging system. Image uniformity, image noise and image resolution are the primary factors affecting image quality in spectral CT and hence they will be investigated in this project.

4.1 Hounsfield Calibration

In order to perform a quality analysis on an image, a Hounsfield Calibration has to first be conducted to convert the attenuation values in the data to correspond to the Hounsfield Unit (HU). The HU is a commonly used unit to present attenuation data, where water is defined as 0 HU, and air is defined as -1000 HU. The calculation for the HU of a material with a linear attenuation coefficient μ is given by Equation (4-1).

$$HU = \frac{\mu - \mu_{water}}{\mu_{water} - \mu_{air}} \times 1000 \tag{4-1}$$

where the linear attenuation coefficients of water and air are represented by μ_{water} and μ_{air} respectively, [*Stephane Sammartino and Capowiez*(2011)].

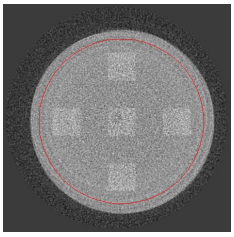

Figure 4.1: The 5 square ROIs for the uniformity test.

4.2 Image Uniformity

The efficiency of a CT scanner at uniformly measuring attenuation across an object has a profound effect on the diagnostic quality of the final image. Image uniformity is degraded by the very nature of the CT scanning and reconstruction processes, wherein the objects that lie at the scanner's periphery are processed differently to those at the centre of rotation. The uniformity is also affected by the number of photon counts at the detector. According to Poisson statistics, as the counts become higher, the relative standard deviation decreases. Therefore the deviation of the photons' energies from the peak of the energy spectrum decreases. This means that the coefficient of variation and the statistical noise are reduced as the number of counts goes up, leading to higher image uniformity. To measure how the image uniformity is affected by different scan parameters, a uniform water phantom was scanned to produce an image. The image was analysed by comparing the HU from its central region of interest(ROI) with the mean HU from its four peripheral ROIs, in order to give a HU difference that was proportional to the uniformity degradation. Figure 4.1 shows the five ROIs of the water phantom image, represented by the five square blocks, which were analysed using MATLAB codes[*Linscott*(2012)].

4.3 Image Noise

The accurate interpretation of an image depends on the amount of image noise present.

Random statistical noise is the main source of noise as an x-ray beam transmits the energy of its photons to the detector. Random noise results in fluctuations of the image density which changes from one image to the next in a fashion that is random and unpredictable, especially when the signal to noise ratio (SNR) is low[*Hanson*(1990)]. The SNR compares the level of the desired signal to the level of background noise, and is displayed in Equation (4-2), where P_{signal} is the power of the signal and P_{noise} is the power of the noise.

$$SNR = \frac{P_{signal}}{P_{noise}} \tag{4-2}$$

Due to the natural statistical fluctuations that arise in the source and in the scattering and absorption processes in the sample, the number of photons that is detected will differ in each subsequent identical measurement[*Sheikh and Bovik*(2005)]. This statistical noise (often called photon noise or photon speckle) increases the graininess of an image and is more pronounced when a thin slice is scanned, or when the x-ray beam contains insufficient energy to penetrate the scanned object.

In conventional detectors, the second source of noise originates from within the electronic circuits of the detector. Due to the nature of Medipix circuitry, this source of noise leads to energy uncertainties[*Sheikh and Bovik*(2005)].

Round-off errors in the digital computer also contribute to the noise introduced in the reconstruction process. Round-off errors result from the use of a limited number of bits in the computer to represent numbers. For example, when a computer represents a number which is a product of two numbers, that number must be rounded off to the least significant bit, which introduces error[*Hanson*(1990)].

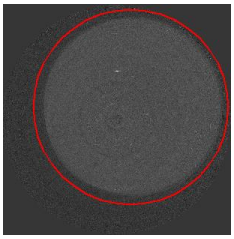

Figure 4.2: The image of a water phantom with an annulus mask applied for noise measurement.

A CT scanner produces a wide variety of artifacts. Artifacts interfere with the interpretation of a CT image and are therefore viewed as a form of image noise. This form of noise often appears in the image as a readily identifiable pattern, for example, the streaking artifact that may be caused by under-sampling, photon starvation or scatter[*Boas and Fleischmann*(2011)]. However, random noise is not produced from these identifiable artifacts, even though the artifacts can cause an increase in the variance inside certain regions of an image[*Hanson*(1990)].

Lastly, structural noise is caused by density variations in the object which the CT scanner cannot differentiate. Even though CT imaging eliminates the structural noise that is associated with the superposition of the various anatomical structures seen in plain film x-rays, it can still be exposed to the partial volume effect. This effect is more pronounced in the images obtained from thick slice scans[*Hanson*(1990)].

For this experiment, the focus of measure was on the statistical noise. This was carried out via the measurement by MATLAB over an annulus mask applied to the image of a completely uniform slice of water (Figure 4.2), of the standard deviation in pixel attenuation values, which was later converted to the standard deviation in HU.

4.4 Spatial Resolution

The ability of a CT system to differentiate small adjacent objects is expressed by its spatial resolution. The resolving power of a CT scanner determines whether or not small objects with very different attenuation values but lie closely together can be differentiated. When scanning an object that contains two small structures with very different densities, the edge between the structures can be assumed to be a signal of high frequency[*McNitt-Gray*(2005)]. However, the CT system cannot resolve a signal of such high frequency, so the signal only appears as a blurred edge in the image, effectively making the two small structures appear as one. If, however, the spatial resolution of the CT system is increased and improved, it would then become capable of imaging such high frequency signals, and the edges between the small adjacent structures would become resolvable and no longer blurred. Transferring this example to a hospital context, the increased spatial resolution of the CT system will enable a clinician to better visualise the presence of any small anatomical abnormalities that may be present in the patient[*Reddinger*(1998)].

For this experiment, an image taken from the slice of a water phantom was used to measure the spatial resolution. The spatial resolution was represented by the 10% modulation transfer function (MTF), which was calculated by a direct analysis of the edge response function of the air/water edge of the water phantom image, after an annulus mask was applied, as shown in Figure 4.3. MTF is a measure of a system's ability to transfer the contrast of an object to the image plane at a specific spatial frequency i.e. resolution, expressed in units of cycles/mm. A higher MTF indicates a higher efficiency at doing so, where a value of 1 indicates that 100% of the contrast information is transferred and a value of 0 indicating that 0% is transferred. The 10% MTF represents the spatial resolution at which there is only a 10% modulation of the transferred contrast[*Linscott*(2012)], where a higher spatial resolution will be characterised by a larger 10% MTF value. The 10% MTF value will be read off from a MTF graph; an example is shown in Figure 4.4.

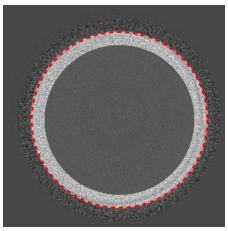

Figure 4.3: The image of a water phantom with an annulus mask applied around the edge for spatial resolution measurement.

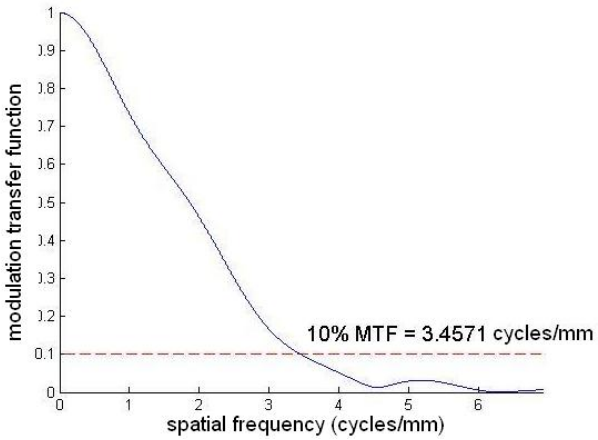

Figure 4.4: A graphical representation for the calculation of the 10% MTF.

4.5 Beam Hardening

The relative high content of low energy photons in the polychromatic x-ray beam degrades image quality by beam hardening. Beam hardening occurs because dense tissues that have high atomic numbers have a tendency to absorb the low energy photons incident upon them, and are only penetrated by the high energy photons that eventually reach the detector. Beam hardening can lead to cupping artifacts in the images scanned from a uniformly attenuating cylindrical water phantom, where x-rays travelling past the middle region of the phantom are hardened more than those travelling past the peripheral regions because the x-rays in the middle region are travelling though more material.

4.6 Summary

Image noise, image resolution and image uniformity, however, can all be substantially improved by making specific changes to the scanning parameters that are used for the acquisition of image data. In the next chapter, the methods that were employed to achieve this will be discussed as well as the results.

Chapter 5

Parameters of CT scanning

In CT scanning, the many components of image quality that were discussed in the previous section are profoundly influenced by various technical parameters. Although a heavy emphasis is placed on image quality, the reduction of the radiation dose to clinically acceptable levels has become an even larger focus.

The purpose of this chapter is to describe the different scanning parameters which consist of the number of projections, tube kVp, mAs, and to describe how each of these may affect the radiation dose and image quality. Particular attention will be given to the tradeoffs that exist in fulfilling the objective of achieving the optimal image quality while minimising the radiation dose.

5.1 Experimental Setup

The object used for the experiments was the water phantom, which is a 30 mm diameter perspex cylinder that contains distilled water, shown in Fig 5.1. It also contains an additional chamber of air along part of its length inside the water. A nylon stopper is placed at its base to allow the emptying and filling of the vessel. A small air bubble is reserved inside the vessel to avoid confusion of the phantom with a solid phantom of another type. Data was obtained from the cross sectional areas of the segment between the two black solid lines containing only water.

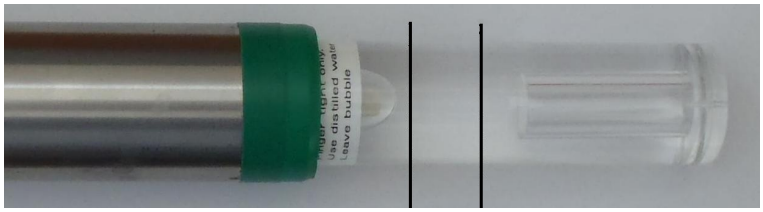

Figure 5.1: A water phantom.

The water phantom was chosen for the experiments because the attenuation value of water closely resembles that of human soft tissue, therefore it gives the most representative information that will be relevant when applied to a clinical context in the future.

A Hounsfield calibration was performed by first scanning the water/air boundary of the water phantom to produce a set of raw data that was then reconstructed to acquire 2D slice images, from which the linear attenuation coefficients of water and air were calculated using MATLAB codes. Those were the two values used when a HU calibration was required for the analysis of the image noise and image uniformity[*Linscott*(2012)].

The CT geometries that are relevant to the experiments are the source-to-object distance (SOD) and the object-to-detector distance (ODD). The SOD measures the distance between the x-ray source and the sample; the ODD measures the distance between the sample and the Medipix3 detector. A magnification (M) of the sample can be achieved in the image by the use of Equation (5-1).

$$M = \frac{(SOD + ODD)}{SOD} \tag{5-1}$$

5.2 Number of Projections

The main parameter of imaging geometry is the number of projections. The number of projections directly affects the quality of the reconstructed CT images. The use of infinite projections allows the specimen to be re-

constructed without mathematical error, but a reduction in the number of projections reduces the scan time, radiation dose and keeps the patient comfortable[*AN van Daatselaar*(2004)]. However, the reduction in the number of projections also reduces the image quality due to a sparser sampling of the sample data. Therefore, the optimal number of projections is a compromise between the image quality and real-life practicality[*Fang Zheng*(2009)].

The purpose of this part of the experiment is to first find the relationship between the number of projections and the reconstructed image quality, then from that determine the number of projections that is necessary to obtain an image of adequate quality while taking into consideration the radiation exposure. The water phantom was used to carry out this experiment, the x-ray tube inside the MARS spectral CT was set to 50 kVp, with a tube current of 0.5 milliamperes (mA), and an x-ray exposure time of 0.1 second. The CT scan consisted of 2400 projections through 360 degrees. With these projections, other scans with less numbers of projections were emulated through the removal of projections using the Python codes written by Dr Judy Mohr. This was done in such a way that the emulated projection series were all nearly equally spaced from each other. The emulated projection series consisted of numbers of projections at 360, 720, 900, 1200, 1440, 1800 and 2400.

After the water phantom was scanned with all the different numbers of projections, the data was preprocessed using the MARSCT builder and then reconstructed using OctopusCT. Finally, the image quality was analysed using MATLAB codes as a function of the number of projections in terms of the image noise, image uniformity and image resolution. It is important to note that, before the image quality analysis was carried out, all the individual reconstructed slices from a dataset were averaged into one single slice that was representative of that whole dataset by using the image processing program ImageJ. This choice was justified by the fact that the image noise values obtained from the use of individual slices did not form any noticeable

trends amongst each other, and their error bars had values of over 1500 HU, which is much larger than even the image noise value itself.

5.2.1 Results

Looking at Figure 5.2, the first image with 360 projections appears extremely grainy. But as the number of projections increases, the images become smoother, with the smoothest looking image at 2400 projections. This trend can be seen in Figure 5.3(a), where it is clearly shown that as the number of projections increases, the noise (standard deviation in HU) exponentially decays across the uniform water phantom. This reduction in noise as the number of projections increases is due to the increased SNR. Increasing the number of projections increases the amount of x-ray signals that register at the detector, while the noise signal does not raise as much, and therefore the overall SNR is improved, resulting in an image that contains less overall noise. The trend in Figure 5.3(b) shows that an increase in the number of projections also results in improved image spatial resolution. This positive trend gradually starts to level off at 900 projections and forms an asymptote at 2400 projections, indicating that the point has been reached where any further increase in the number of projections will no longer affect the image spatial resolution. However, Figure 5.3(c) shows that a clear relationship between the number of projections and image uniformity does not exist.

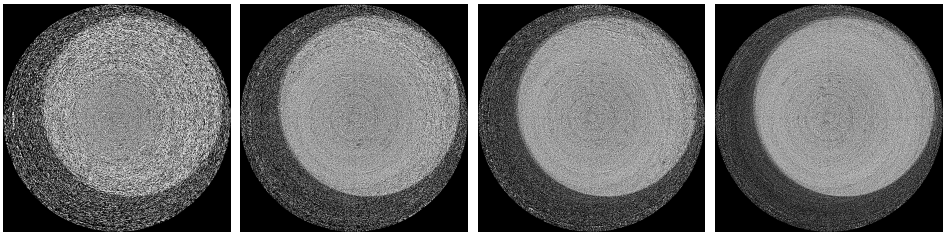

(a) 360 projections (b) 720 projections (c) 900 projections (d) 1200 projections

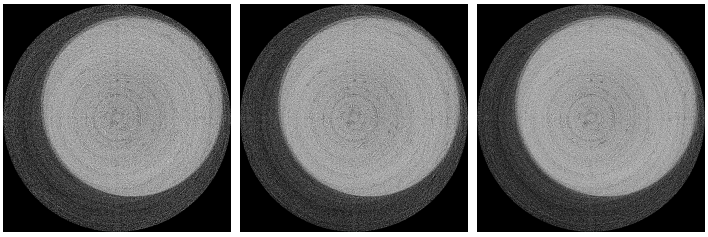

(e) 1440 projections (f) 1800 projections (g) 2400 projections

Figure 5.2: OctopusCT reconstructed water phantom images from scans taken at different numbers of projections.

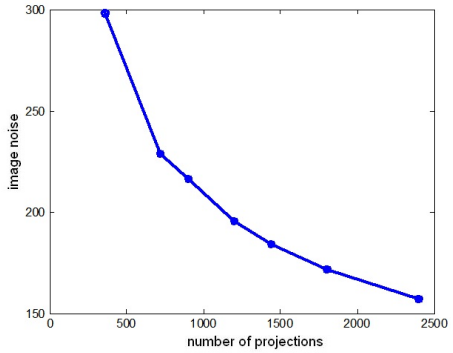

(a) Number of projections vs image noise.

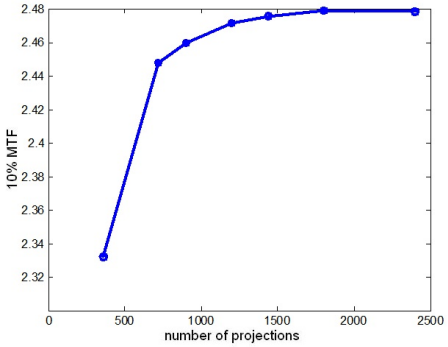

(b) Number of projections vs image spatial resolution.

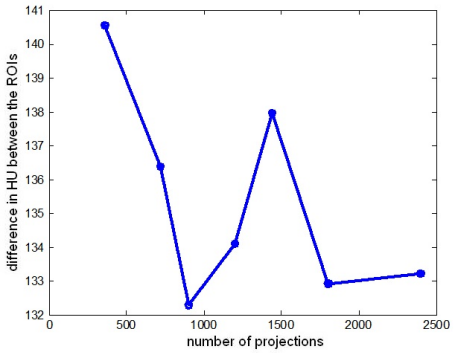

(c) Number of projections vs image uniformity.

Figure 5.3: The relationship between the number of projections and the different aspects of image quality.

Even though these results suggest that there exists a positive relationship between the number of projections and overall image quality, with the image of best quality obtained at 2400 projections, scanning at 2400 projections also takes up the most amount of time and delivers the most amount of radiation to the sample. In addition, prolonged scanning using 2400 projections can damage the Medipix3 detector. Based on these drawbacks, it was decided to set the compromise between the best image quality and lowest possible dose to be at 1440 projections, where its noise value of 184.40 HU lies well below the 298.32 HU obtained from the 360 projection scan, and is only 27.45 HU higher than that obtained from the 2400 projection scan. The value of spatial resolution (2.476 cycles/mm) from the 1440 projection scan is also extremely close to that of the maximum spatial resolution (2.479 cycles/mm) from the 2400 projection scan.

5.3 Tube kVp and Detector Threshold Energy (kV)

The tube kVp is an important parameter in CT imaging but its optimal settings for the MARS spectral CT is not yet well established. The number of x-ray photons produced increases as the tube kVp increases. Unlike the linear relationship that is observed when the tube current is changed (discussed in the next section), a doubling of the tube kVp produces a four-fold increase in the total number of x-ray photons emitted i.e. the tube output is proportional to the square of kVp[*Ogden*(2011)].

An increase of the tube kVp will also lead to an increase in the average photon energy, leading to reduced levels of x-ray attenuation. The attenuation coefficients are expressed in HU, which is a measure of the amount of attenuation of a sample relative to that of water. So if a lesion was to be surrounded by water, the value of the lesion HU would quantify the relative difference (contrast) between the x-ray attenuation of the lesion and that of the surrounding water. Generally, a change in the x-ray energy will also lead to a change in the HU of a tissue, so changing the tube kVp will also change

the amount of contrast in the resulting image [*Fang Zheng*(2009)].

The purpose of this part of the experiment was to investigate the image quality of the reconstructed images at various peak tube voltages. As above, a water phantom was once again used; the tube current remained at 0.5mA, and the exposure time at 0.1 second. The CT scans consisted of 360 projections through 360 degrees, with measurements taken for different tube kVp at 30, 40 and 50 kVp. In addition, to observe how different detector threshold energies affected the quality of the images, for the 50kVp scans, threshold energy values from 15kV to 45kV with 10kV intervals were used; for the 40kVp scans, values from 15kV to 35kV with 7.5kV intervals were used; and for the 30kVp scans, values from 15kV to 25kV with 2.5kV intervals were used. The reconstructed images from these scans were averaged by ImageJ and analysed using MATLAB codes.

5.3.1 Results

From the three sets of images in Figures 5.4, 5.5 and 5.6, as the detector threshold energy increases for the same tube kVp, the image becomes noisier and less uniform. However, when scans are conducted at different tube kVp but the same threshold energy settings, the images from the higher tube kVp scans appear less noisy and more uniform than those from the lower tube kVp scans. The trends seen in Figures 5.7 and 5.8 confirm with this phenomenon. Figure 5.9 shows that a consistent relationship does not exist between the 10%MTF and different tube kVp/detector threshold energy settings, so their relationship to each other will not be discussed any further.

The highest tube kVp (50kVp) produces images with the least amount of noise and the best uniformity at all the different detector threshold energies. This is due to the higher number of photons that is produced by the high tube kVp than is produced by the low tube kVp, which leads to a higher SNR and consequently, less noise and more uniformity.

In the group of images that were obtained from scanning with the same

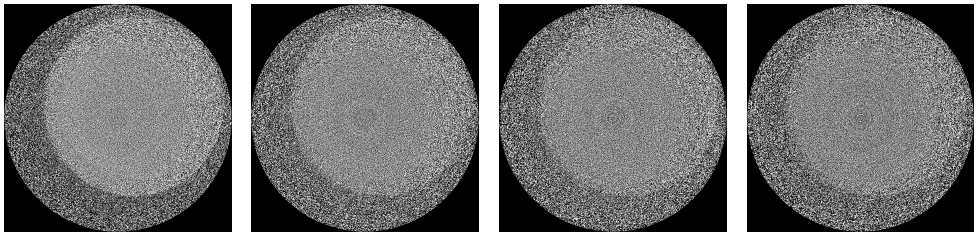

(a) 15kV (b) 20kV (c) 22.5kV (d) 25kV

Figure 5.4: OctopusCT reconstructed water phantom images from scans taken at 30kVp with different threshold energies.

tube kVp, the image that is scanned at the lowest detector threshold energy had the least amount of noise. The reason this was observed is because of the fact that the x-rays emitted at the user specified tube kVp are actually made up of a full spectrum of energies. In other words, the user-specified tube kVp serves only as a cut-off point, and is not representative of the energies that most of the photons in the energy spectrum possess. Raising this detector threshold energy increases the image noise because of the decrease in SNR caused by the dismissal of x-ray photons of energies below that of the detector threshold energy, which according to the results, forms a great proportion of the signal. This effect becomes more noticeable as the detector threshold energy approaches the tube kVp, where almost all of the photons possess energies that lie below that of the detector threshold and as a consequence do not register on the detector. However, as the tube kVp is raised higher above the same detector threshold energy, the average energy of the x-ray spectrum becomes shifted higher, and no longer cut off by the detector threshold; this results in less photon removal from the main x-ray spectrum, giving a better SNR and image quality.

These results suggest that the optimum image quality is achieved when the tube kVp is set to 50kVp with the detector threshold energy set to 15kV.

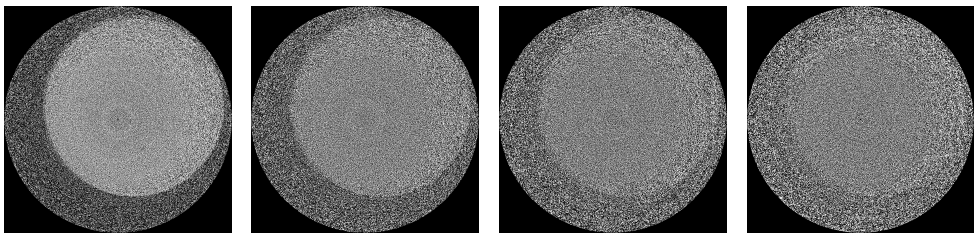

(a) 15kV (b) 25kV (c) 30kV (d) 35kV

Figure 5.5: OctopusCT reconstructed water phantom images from scans taken at 40kVp with different threshold energies.

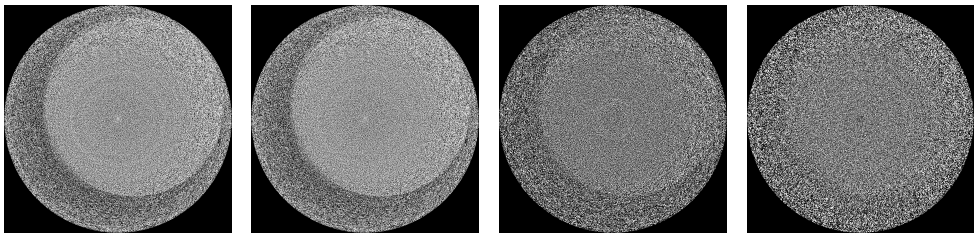

(a) 15kV (b) 25kV (c) 35kV (d) 45kV

Figure 5.6: OctopusCT reconstructed water phantom images from scans taken at 50kVp with different threshold energies.

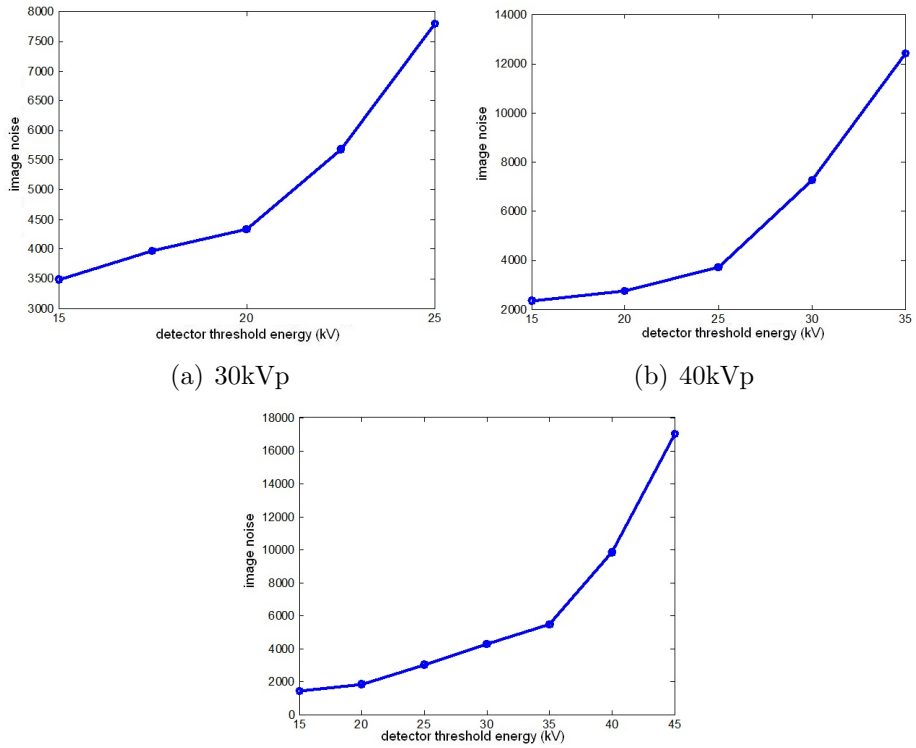

(a) 30kVp (b) 40kVp

(c) 50kVp

Figure 5.7: Detector threshold energy (kV) vs image noise at different tube kVp.

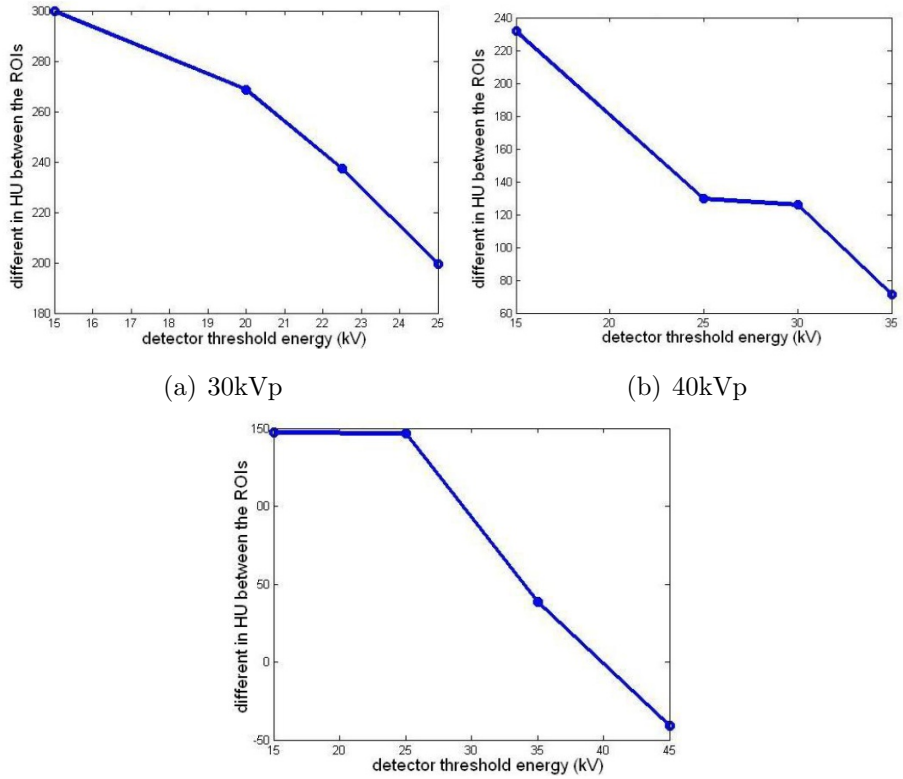

(a) 30kVp (b) 40kVp

(c) 50kVp

Figure 5.8: Threshold energy vs the difference in HU between the central and peripheral ROIs at different tube kVp.

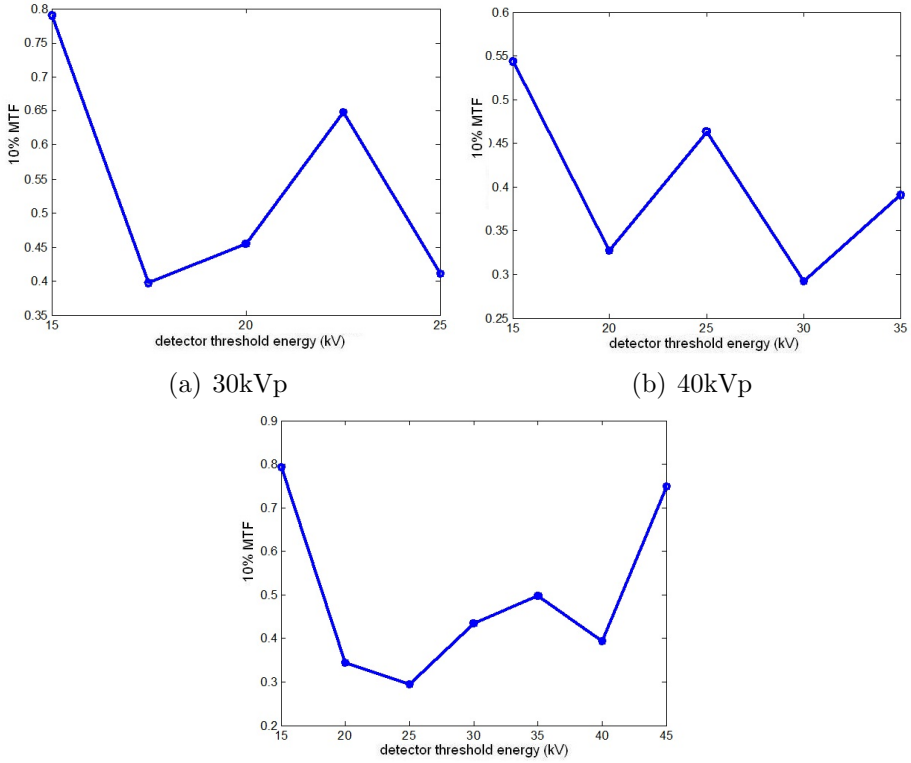

(a) 30kVp (b) 40kVp

(c) 50kVp

Figure 5.9: Detector threshold energy vs image spatial resolution at different tube kVp.

5.4 Exposure Time Product

The rate at which x-ray photons are produced in the x-ray tube, i.e. photons per second, is determined by the x-ray tube current. The total number of photons that are detected by the Medipix detector in a single exposure is related proportionally to the product of the rotation time in seconds and the tube current in mA, the exposure time product (mAs). Increasing the mAs reduces the image noise, because the random statistical noise is inversely proportional to the square root of the number of photons reaching the detector. This means, the noise in a CT image will be halved if the exposure time product is quadrupled [*John A. Mayo*(1995)]. However, the exposure time product should always be kept as low as reasonably achievable to reduce the radiation dose delivered to the patient. When at a fixed tube kVp and exposure time, the radiation dose displays a linear relationship to the tube current, so therefore increasing or decreasing the current component of the exposure time product is equivalent to an increase or decrease in dose, respectively [*John A. Mayo*(1995)].

Selecting the appropriate exposure time product is crucial, because an excessive exposure time product transmits too many photons through the sample to the detector. This has the effect of neglecting the sample attenuation, and results in pixel saturation at the detector, which means that all the pixels are saturated with the maximum number of photon counts, and a dark image results. Therefore the optimal value for the exposure time product is an appropriate balance between delivering the minimal radiation dose while obtaining consistently good quality images, and avoiding over-exposure induced pixel saturation[*Fang Zheng*(2009)].

Since there was no consensus on the optimal exposure time product for scans using the MARS spectral CT, the purpose of this part of the experiment was to find the optimal value for this parameter. The uniform water phantom was used once again. All the images were scanned at 360 projections through 360 degrees, at a tube current of 0.5mA and a tube kVp of 50 kVp. The

SOD was set to 130 mm, and the ODD set to 88.4 mm to give a magnification factor of 1.68. The exposure time was selected to be the changing variable. Five sets of data were taken at exposure times of 100ms, 500ms, 1s, 1.5s, 2s, corresponding to exposure time products of 0.05mAs, 0.25mAs, 0.5mAs, 0.75mAs and 1mAs, respectively. The reconstructed images from these scans were averaged by ImageJ and analysed using MATLAB codes.

5.4.1 Results

The scans from this part of the experiment are displayed in Figure 5.10, and their values of image noise, image resolution and image uniformity at different mAs are plotted in Figures 5.11(a), 5.11(b) and 5.11(c), respectively. Figures 5.11(a) and 5.11(c) show that the image from the highest mAs scan (1mAs) has both the best noise and uniformity values. However, even though both the noise and uniformity values of the 0.5mAs exposure scan are worse than those of the 0.75mAs and 1mAs exposure scans, the 0.5mAs exposure scan gives the image with the best visual contrast and spatial resolution out of all the five images, as indicated in Figure 5.11(b). This is due to the fact that a larger proportion of the detector pixels representing the final two images are saturated with photons during the scan. When the exposure time product is increased, a greater proportion of the photons passes through the phantom and is registered on the detector, to the point where some of the pixels on the detector reach their maximum number of photon counts, rendering any further photon counts unregistrable, causing saturation. A graphical representation of the detector pixel saturation is shown in Figure 5.12, where the saturated photon counts are represented by a single vertical bar that is located to the right-side edge of each bar graph. The number of saturated pixels becomes more numerous as the exposure time product increases, which indicates that a greater proportion of the detector pixels are saturated and image further degraded.

The image obtained from the 0.5mAs exposure scan with a 1.68 magni-

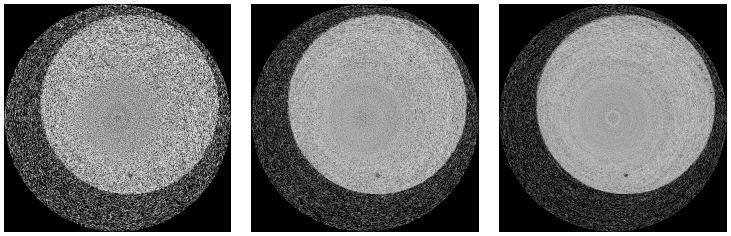

(a) 100ms exposure (b) 500ms exposure (c) 1000ms exposure

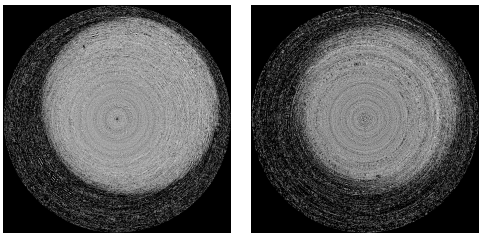

(d) 1500ms exposure (e) 2000ms exposure

Figure 5.10: OctopusCT reconstructed water phantom from scans taken at different exposure time products.

fication factor shows the highest spatial resolution value of 2.75 cycles/mm and the best balance between the image noise and pixel saturation, where its noise value of 345.21 HU lies much below that of the maximum value of 908.67 HU while approaching that of the minimum value of 301.64 HU; this gives the image with the best quality.

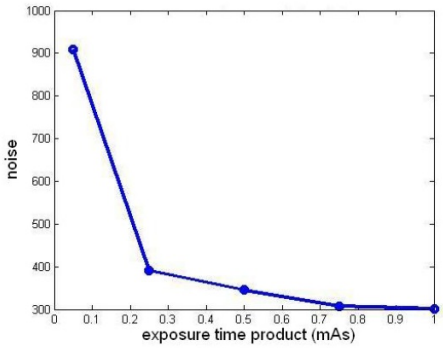

(a) The variation of the noise as a function of the exposure time product.

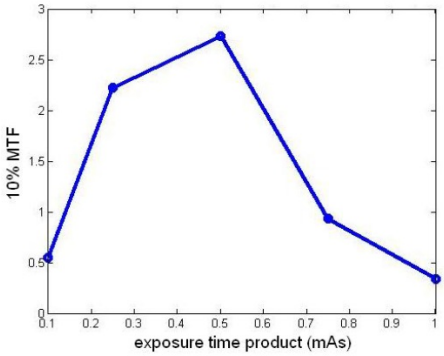

(b) The variation of the image spatial resolution as a function of the exposure time product

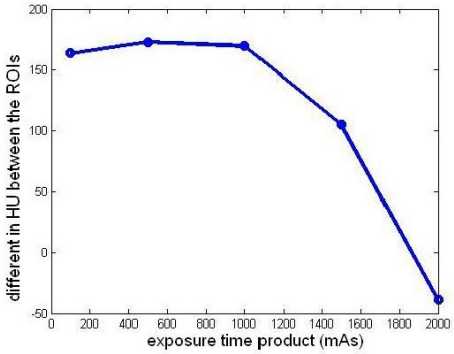

(c) The variation of the difference in HU between the central and peripheral ROIs as a function of the exposure time product.

Figure 5.11: The relationship between the exposure time product and the different aspects of image quality.

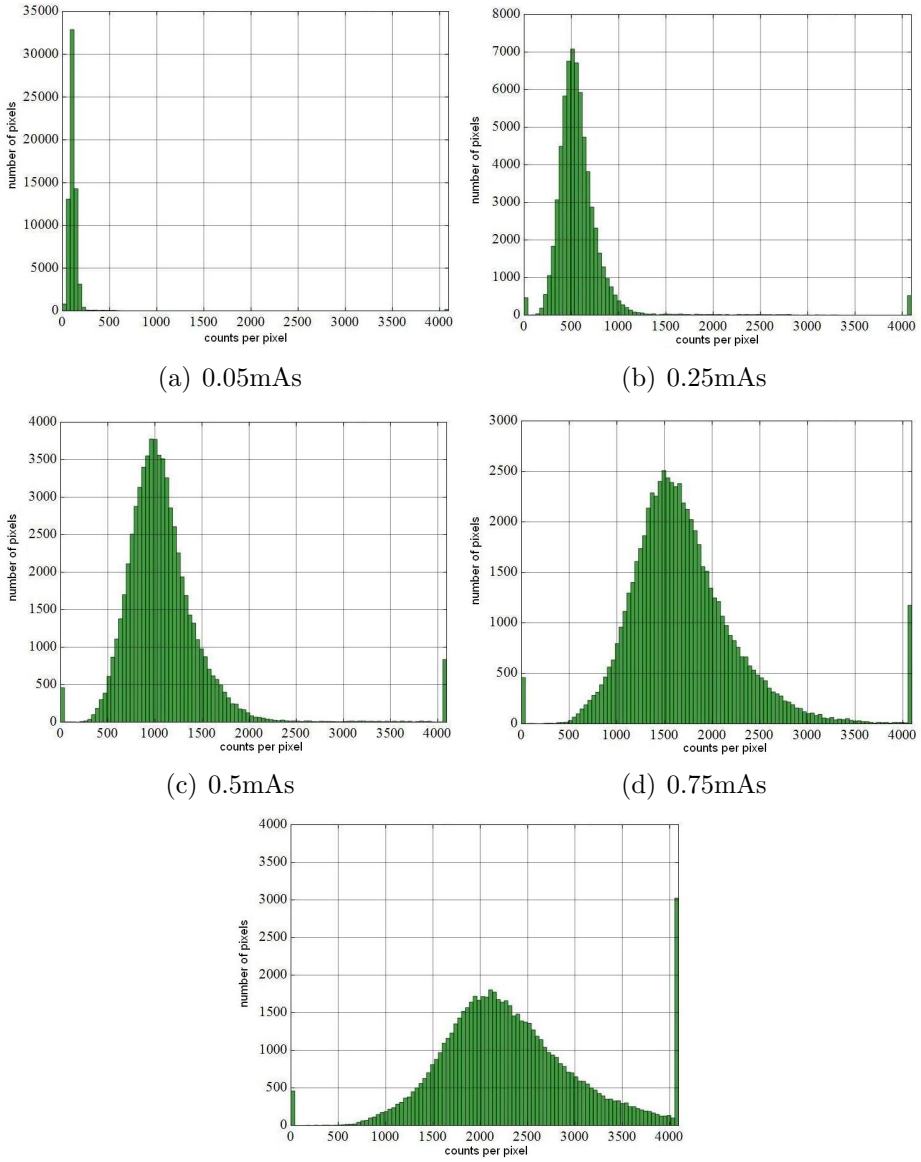

(a) 0.05mAs

(b) 0.25mAs

(c) 0.5mAs

(d) 0.75mAs

(e) 1mAs

Figure 5.12: Distribution of count rates on the detector pixels for scans taken at different exposure time products.

5.5 Practical Implications

Given the results from the graphs in the previous sections, it is concluded that the best compromise between the image quality and radiation dose for scans using the MARS spectral CT with the silicon quad Medipix 3.0 detector can be achieved by setting the scan parameters to the values listed in Table 5.1. These parameters can be effectively applied to most biological samples that are scanned in the MARS spectral CT due to the similarity of their sizes to the water phantom.

The water phantom and the abdominal cross-section of a mouse were scanned using the optimal scan parameters and are displayed in Figures 5.13 and 5.14. The image of the water phantom gives the noise, spatial resolution and difference in the uniformity of the ROIs values as 91.72 HU, 1.41 cycles/mm and 60.47 HU, respectively. These image quality values form a combination that is superior to any of those that were obtained from the images in the previous sections. In addition, the abdominal cross-section of the mouse obtained from the optimal scan parameters displays superb detail and shows crisp clear edges of the spine, stomach and limb. Figure 5.15 shows the 3D image that was reconstructed from the abdominal cross-sectional slices of the mouse abdomen, showing an excellent and almost noiseless 3D view of the spine with high resolution, where even the tiny holes on the vertebrae in which the blood vessels enter can be clearly seen. These confirm with the fact that the optimal scan parameters for the Medipix3.0 silicon quad detector have been well chosen.

Table 5.1: Optimal scan parameters for the Medipix3.0 silicon quad detector.

Scan Parameters	Optimal Settings
Number of Projections	1440
Peak Tube Voltage (kVp)	50
Threshold Energy (kV)	15
Exposure Time Product (mAs)	0.5 at 1.68M

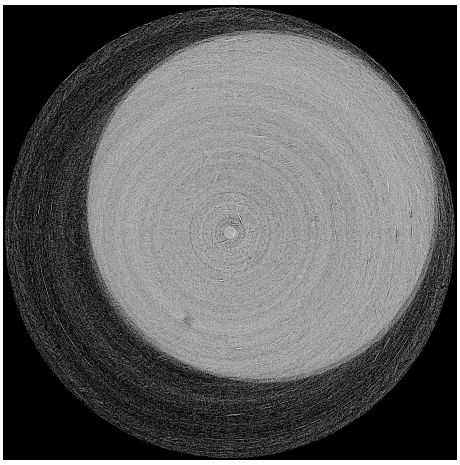

Figure 5.13: The image of a water phantom that was reconstructed from a scan using the optimal scanning parameters.

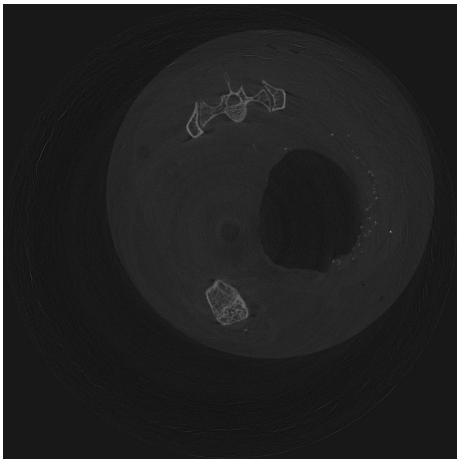

Figure 5.14: The image of the abdominal cross-section of a mouse that was reconstructed from a scan using the optimal scanning parameters.

Figure 5.15: A 3D visualisation of the mouse abdomen using the data obtained by using the optimal scanning parameters.

Chapter 6

mART vs OctopusCT

This chapter focuses on the new reconstruction software mART that utilises the algebraic reconstruction technique (ART). This software was created by Niels de Ruiter, in which I was involved in the analysis of the quality of its reconstructed images against that of OctopusCT which uses the filtered back-projection technique (FBP). In addition, I coordinated efforts on writing this work into a scientific publication where I also wrote as the lead author, which was later presented at the Imaging and Vision Computing New Zealand Conference 2012.

To maximise the potential of spectral CT, many new image processing techniques for reconstruction, material decomposition and visualisation are now in development. A small application called mART which implements a Simultaneous Algebraic Reconstruction Technique (SART) was created by Niels de Ruiter from the MARS team, and is expected to be extended for spectral reconstruction[*Andersen and Kak*(1984)]. This chapter will detail the preliminary work completed before the development of a spectral reconstruction algorithm may be considered. An overview of mART will be given, and then a comparison of the quality of the reconstructed CT images by mART and OctopusCT (the current commercial software used by the MARS team) will be shown.

One of the key reasons leading to the success of the MARS spectral CT lies in the image processing of spectral CT data with reconstruction algorithms,

which has the potential to exploit the nature of spectral CT data, improving image quality and reducing radiation dose.

OctopusCT developed by InCT systems is the current reconstruction software adopted by the MARS team[*inCT*(2012)]. OctopusCT is a commercial application that uses a FBP algorithm[*Budinger and Gullberg*(1974)]. It reconstructs data from the MARS spectral CT by reconstructing every acquired energy bin independently. Despite its success, this method of reconstruction ignores the spectral component of the data. In addition, FBP only works well for high dose scans, which is counter-productive to the goal of the MARS team.

SART serves as a simple and flexible basis that will be extended for spectral reconstruction in the near future. In this study, it was concluded that OctopusCT can be suitably replaced by mART. Image reconstructions by both OctopusCT and mART on single energy scans were analysed and compared. It was shown that mART produces images of superior quality to those of OctopusCT, especially for low dose scans.

6.1 Overview of ART

6.1.1 Algebraic Reconstruction

Johann Radon first introduced the theory behind reconstruction algorithms in 1917[*Radon*(1917)]. His work involved a mathematical procedure that uses the inverse Radon transform to recreate a subject image from many projection images. However, the inverse Radon transform does not have an analytical solution in its basic state. Bates and Peters found a solution to this problem in 1971 by using Fourier transforms, which became known as FBP[*Bates and Peters*(1971)]. Due to its high computational efficiency, FBP rapidly became the solution of choice after the CT scanner was commercialised in 1972 by Godfrey Hounsfield[*Hounsfield*(1973)].

An algebraic solution is another common reconstruction approach. This

approach maps the reconstruction problem into a simple linear algebraic equation shown in Equation (6-1).

$$A\boldsymbol{x} = \boldsymbol{b} \tag{6-1}$$

This mapping can be achieved by using the Beer Lambert Law shown in Equation (6-2). It relates the measured photon counts C to the transmission μd along a single ray from the source to the detector element when the initial photon counts C_0 is known.

$$C = C_0 e^{-\mu d}. \tag{6-2}$$

The transmission can be broken down into a sum of smaller steps as shown in Equation (6-3), where it can be seen that it is of the same form as Equation (6-1), where $\boldsymbol{b}$ is equivalent to the measured transmission ($\mu_T d_T$) calculated from the Beer Lambert Law, $\boldsymbol{x}$ is equivalent to the linear attenuation elements (μ_i) that make up the volume, and A is equivalent to the contribution of every volume element from $\boldsymbol{x}$ to a detector element in $\boldsymbol{b}$ along a ray (d_i).

$$\mu_T d_T = \sum \mu_i d_i. \tag{6-3}$$

However, Equation (6-1) is under-determined and cannot be solved analytically, which does not aid in dose minimization with fewer exposures. Therefore, iterative techniques have been explored to find a good solution, namely the Kaczmarz Equation [*Kaczmarz*(1937)] as illustrated in Equation (6-4).

$$\boldsymbol{x}_k = \boldsymbol{x}_{k-1} + \frac{\boldsymbol{b}_k - \boldsymbol{x}_{k-1} \cdot \mathbf{A}_i}{\mathbf{A}_i \cdot \mathbf{A}_i} \cdot \mathbf{A}_i \tag{6-4}$$

Despite its effectiveness, different versions of this equation were developed to improve the results. The first one was the Simultaneous Iterative Re-

construction Technique (SIRT) that Gilbert proposed in 1972[*Gilbert*(1972)]. SIRT combines the results from all detector elements that contribute to the voxel in the scan, in order to update the voxel values $\boldsymbol{x}_k$. This significantly increased the reconstruction time but provided results of superior quality.

Proposed by Anderson and Kak in 1984, the Simultaneous Algebraic Reconstruction Technique (SART) is another variation and is similar to SIRT[*Andersen and Kak*(1984)]. In this variation, all the detector elements from a single projection that contributes to a voxel combine to give the voxel updates.

One different approach is the Multiplicative Algebraic Reconstruction Technique (MART) that Gordon proposed in 1970[*Gordon et al.*(1970)]. MART adopts a multiplicative solution while the other iterative algorithms are additive solutions. This in turn has important consequences. Firstly, due to the MART algorithm's simpler structure, it converges faster. Secondly, zero-valued voxels don't have the ability to converge. Lastly, additive methods tend to average the noise while MART tends to magnify the noise.

In recent times, developments in ART have shifted in favour of compressed sensing techniques away from iterative solutions[*Chen et al.*(2008)]. Compressed sensing techniques reduce the amount of data required to reconstruct a signal by applying known constraints to the system, which can greatly reduce radiation dose for images of the same quality. The disadvantages are low computational efficiency and high complexity.

6.1.2 A Basis for Spectral Reconstruction

Extending an existing algorithm is the simplest approach to develop a new algorithm. Therefore the existing algorithm must be flexible enough to adapt to the new changes. The MARS spectral CT produces datasets that have a few important features. Firstly, the different energy bins are represented by multiple values that are produced by each detector element. Secondly, identical spatial information is yielded by acquiring each energy bin over the

same field of view. Thirdly, new scanning modes such as circular and helical scans with start-stop and continuous motion have been included in recent developments with the MARS spectral CT.

As such, in order to extend a basis algorithm for the needs of the MARS spectral CT, it must be capable of handling custom data structures, prior knowledge, constraints and be flexible in dealing with the scanner geometry.

Out of all the reconstruction algorithms that were mentioned in the previous section, the best balance between speed, simplicity, flexibility and quality is offered by SART[*Andersen and Kak*(1984), *Guan and Gordon*(1996)]. SART is simple like all variants of the Kaczmarz equation. The reconstruction is divided into two basic steps where customization is allowed by each step.

In the first step, the scan is simulated by forward projecting an estimate of the volume, which is perfect for incorporating prior knowledge and speeding up the reconstruction process.

In the second step, a correction factor is generated by comparing the simulation to the measured data. The estimate is then improved by back projecting the correction factor onto the volume. Both the quality and speed of convergence are directly affected by how the correction factor is distributed over the volume. This process may also be improved with spectral knowledge.

Matrix A from Equation (6-1) is heavily relied upon by both the forward and back projection steps. The contribution of each volume voxel to the element in the detector is defined by this matrix. The scanner geometry directly determines this contribution, which means that all the recent developments of the MARS spectral CT can be easily incorporated into SART with minimal effort.

To summarise, SART forms a good basis for the development of a spectral reconstruction algorithm. However, it must first be proven that the implementation of SART is a superior alternative to OctopusCT which is the current commercial reconstruction software used by the MARS team.

This will ensure that sources of errors are eliminated when the algorithm is extended for spectral CT.

6.1.3 mART's Implementation of SART

mART developed by Niels de Ruiter simply implements SART and serves as a modular platform for spectral reconstruction. However, many components of SART is implementation specific, such as the calculation of matrix A.

Matrix A is derived from the scanner geometry. This allows a ray to be cast by informing SART of the position of the source and the detector element. In mART, a series of 3D translations and rotations model the scanner geometry so that no assumptions are made about the position and orientation of the detector. The transformations include detector and sample translations, magnification, rotation of the gantry, and skew angles associated with any translations. Therefore, as long as the scanner knows its position with sub-pixel accuracy, then the reconstruction will function with any set of arbitrary positions (circular, helical, etc).

mART reconstructs energy bins independently in its current form. However, the initial estimate for other energy bins are determined by the reconstruction of the broad spectrum. This allows the reconstruction process to be sped up because it exploits the fact that spatial data is the same between different energy bins.

A suitable pre-processing chain allows sufficient implementation of the reconstruction algorithm. Pre-processing chains include masking of bad detector elements, flatfield normalization, correction of bad detector elements (inpainting), and stitching of detector frames into a projection image.

Knowledge of the initial counts at the source (C_0 from the Beer Lambert Law) is required to calculate the transmission values, and may be estimated by scanning the air (flatfielding). This estimation works well as a flatfield and also contains information about the state of the beam and chip. Therefore, the image quality is improved and part of the conversion into transmission

data is formed by the flatfield normalization.

However, dead, unstable detector elements or quantum noise are not accounted for by the flatfield. Therefore it is crucial for the bad detector elements to be identified. The pixels that vary beyond n standard deviations (n is user defined) can be eliminated because the dominant noise forms a poisson distribution due to the fact that the MARS spectral CT operates by counting photons. Also, scanning and taking measurements without an x-ray source (darkfielding) provides a map of dead pixels. Together, the creation of a reasonable mask can be achieved.

The stitching and inpainting form the primary difference in pre-processing between FBP and ART. In FBP, the full set of data from a single projection is required because it works in the Fourier space. However, ART operates on individual detector elements, meaning that neither stitching nor inpainting is required, and bad detector elements can simply be ignored.

Therefore, in the pre-processing chain of mART, the raw data is translated into transmission values and all the bad detector elements are simply masked. Whereas in the pre-processing chain of OctopusCT, extra stitching and inpainting techniques are required in order to produce complete projection images.

In summary, a minimalistic approach to pre-processing is employed by mART before using SART for reconstruction; the processing time is reduced because both the stitching and inpainting algorithms are eliminated and the associated interpolation errors avoided.

6.2 Measuring Image Quality

Reconstructions from mART and OctopusCT on both simulated and real data of standard phantoms for a single energy bin in terms of the image noise and image resolution will be compared. All images that are presented in this section have been normalised to HU.

The Shepp-Logan phantom is used in a variety of tomographic medical

imaging applications as a standard simulated phantom. The 3D modified Shepp-Logan algorithm was used by MATLAB to simulate the synthetic Shepp-Logan phantom images. A uniform region of the phantom's interior was selected to determine the attenuation value of water because the phantom did not contain any specific regions of water, and a region of the surrounding medium was selected to determine the attenuation value of air.

Reconstructed slices of the Shepp-Logan phantom using OctopusCT and mART with 72, 180 and 360 x-ray projection scans are shown in Figure 6.1. At 72 projections, OctopusCT results in images with a rippled pattern, but at 360 projections, images from both OctopusCT and mART appear similar.

The measured noise and spatial resolution values for the mART and OctopusCT reconstructions are shown in Tables 6.1 and 6.2, respectively. The values are determined from the average of 10 neighbouring slices in the 3D reconstructed volume. In both cases, the noise in the images decreases as the number of projections increases, which is reflected in Figure 6.1. Even though no statistical difference exists in the image noise between the mART and OctopusCT reconstructions at 360 projections, at 72 projections the mART reconstructions contains approximately half as much noise as those from OctopusCT, which can be seen in Figure 6.1(a) as the enhanced rippling, indicating a higher deviation in the attenuation across the OctopusCT reconstructed slice. Because of this, it may be possible to deliver a lower x-ray dose to a hospital patient by utilising a smaller number of projection, and thus reducing the patients' radiation exposure. The patient may now also be able to undergo more scans before accumulating the same amount of radiation dose that would have accumulated in just one scan had the old reconstruction method been used.

The spatial resolution is independent of the number of projections regardless of which reconstruction method is used. But finer edge details are produced by OctopusCT compared to mART, with the 10%MTF values being $\sim$4.7 cycles/mm and $\sim$2.9 cycles/mm respectively.

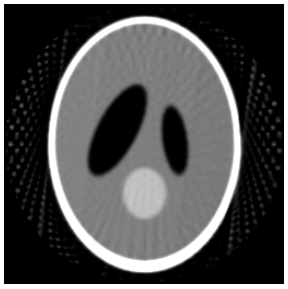

(a) OctopusCT; 72 projections

(b) mART; 72 projections

(c) OctopusCT; 180 projections

(d) mART; 180 projections

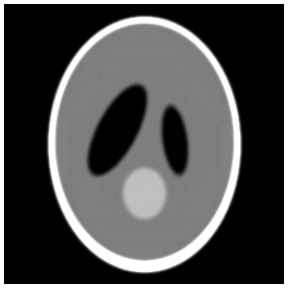

(e) OctopusCT; 360 projections

(f) mART; 360 projections

Figure 6.1: Reconstructed Shepp-Logan Slices.

Table 6.1: Noise and spatial resolution values for mART reconstructions of Shepp-Logan images. 10% MTF values are in cycles/mm.

Shepp-Logan	Noise(HU)	10% MTF
72 projections	4.67 ± 1.92	2.91 ± 0.25
180 projections	2.12 ± 0.90	2.95 ± 0.26
360 projections	1.45 ± 0.70	2.95 ± 0.27

Table 6.2: Noise and spatial resolution values for OctopusCT reconstructions of Shepp-Logan images. 10% MTF values are in cycles/mm.

Shepp-Logan	Noise(HU)	10% MTF
72 projections	10.03 ± 4.55	4.16 ± 1.46
180 projections	3.25 ± 1.61	4.74 ± 1.6
360 projections	1.33 ± 0.51	4.74 ± 1.6

Scanned images of a cylindrical water phantom using a silicon quad Medipix 3.0 chip were used to assess the performance of the implemented SART algorithm on real data. To minimise dose, the scans were taken with a short exposure time. Figure 6.2 shows selected slices from the reconstructions, with Tables 6.3 and 6.4 indicating the image noise and spatial resolution.

The graininess of the images in the mART reconstructed slices becomes less prominent as the number of projections go up from 72 to 180 and 360, reflecting the decreasing noise values. However, as the number of projections increases, the 10% MTF value (spatial resolution) decreases. This can be seen from the images at 360 projections having blurrier edges than those of the images at 180 and 72 projections, which demonstrates that smoothing can blur edge definition.

The image reconstructed with OctopusCT using 72 projections in Figure 6.2(a) appears to be extremely grainy with a noise value of 427.52 ± 136.61 HU, and it is difficult for any clear details in it to be seen. But as the number of projections is increased to 180 and 360, the graininess significantly decreases, which matches the measured noise values. However, in the images

Table 6.3: Noise and spatial resolution values for mART reconstructions of a cylindrical water phantom. 10% MTF values are in cycles/mm.

Water Phantom	Noise(HU)	10% MTF
72 projections	211.43 ± 85.37	2.92 ± 0.23
180 projections	124.38 ± 39.97	2.72 ± 0.16
360 projections	98.83 ± 35.63	2.65 ± 0.12

from 180 to 360 projections, the smoothness around the phantom edges are similar to each other, with the 10% MTF value being ∼2.4 cycles/mm.

Generally, mART produces images that are less grainy than those of OctopusCT, but with less defined edges of features. This is because the FBP algorithm of OctopusCT accentuates the high frequency signals which contain most of the noise during image reconstruction, and this results in the exaggerated graininess that is seen in the image. In contrast, the iterative ART algorithm reconstructs the low frequency signals first and then moves to the higher frequencies. Therefore with ART, there is a choice to stop iterating before the higher frequency signals that cause the noise are reached. However, these high frequency signals also contain edge information, so by stopping the reconstruction before these frequencies are reached, the edges will not be as sharp as they could be. Nonetheless, it is important to note that even if mART keeps iterating, its image noise would still be less than those obtained from OctopusCT. The numbers of iterations performed in both tests were set so that it took about 1 to 2 hours for the reconstructions to complete, and the superior image quality of mART's reconstruction at fewer projections shows that it outperforms OctopusCT.

Reconstructed slices of an atheroma using OctopusCT (left) and mART (right), scanned at 720 projections with a CdTe detector is shown in Figure 6.3, and is HU normalised. A calcified feature is indicated with a bright section (HU 2500) in the atheroma that is located toward the bottom left of the sample. Water, air and various concentrations of calcium chloride and gold fill the surrounding capillaries. The mART reconstructed image appears

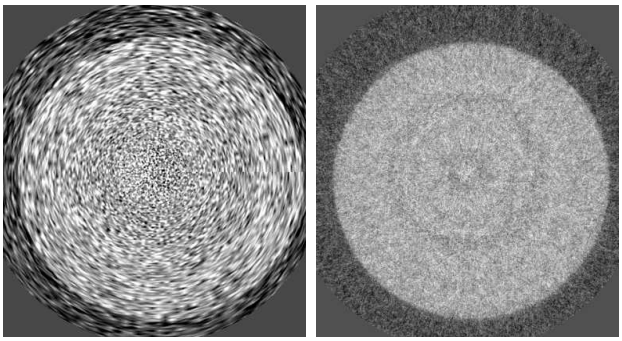

(a) OctopusCT; 72 projections

(b) mART; 72 projections

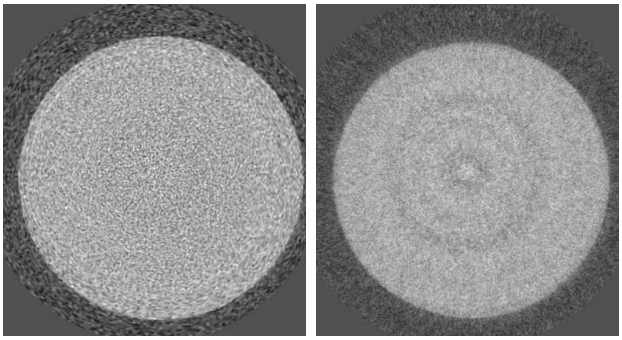

(c) OctopusCT; 180 projections

(d) mART; 180 projections

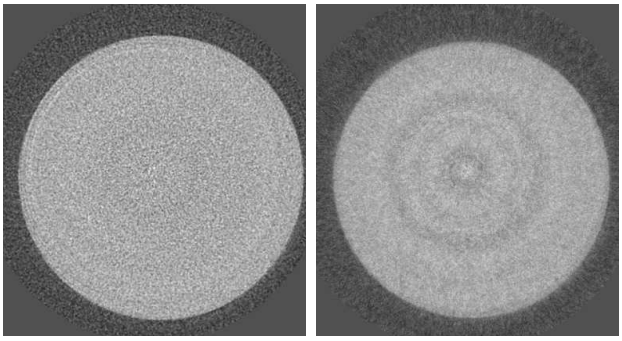

(e) OctopusCT; 360 projections

(f) mART; 360 projections

Figure 6.2: Reconstructed water phantom Slices.

Table 6.4: Noise and spatial resolution values for OctopusCT reconstructions of a cylindrical water phantom. 10% MTF values are in cycles/mm.

Water phantom	Noise(HU)	10% MTF
72 projections	427.52 ± 136.61	0.74 ± 1.40
180 projections	208.48 ± 97.12	2.42± 0.11
360 projections	151.55± 82.89	2.44 ± 0.08

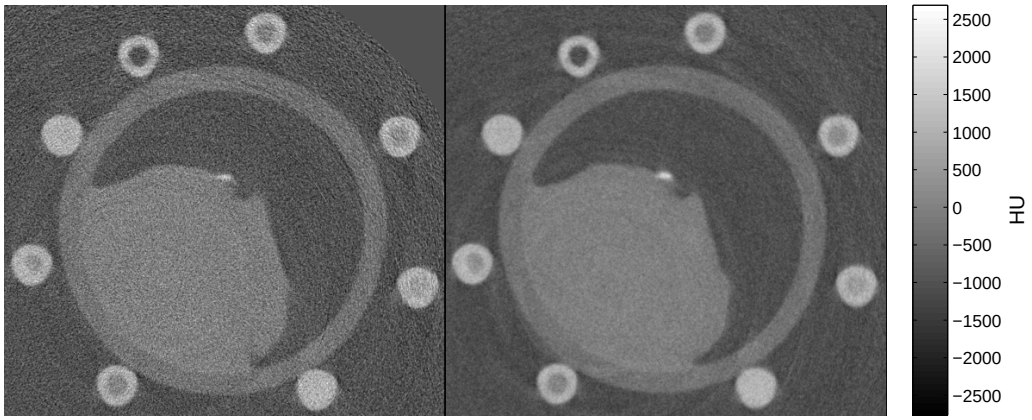

Figure 6.3: Reconstructed slice of an atheroma. Image on left is reconstructed using OctopusCT, whereas image on right is reconstructed using mART. Both images are scaled to HU units.

to be less grainy than that of OctopusCT, which agrees with the general values obtained from the quality analysis on the images of the Shepp-Logan and water phantom. However, even though the OctopusCT reconstructed images appear to be less smooth and more grainy, they have a less blurry edge compared to those of mART, which is in agreement with the differing spatial resolution values that were observed earlier, showing that the OctopusCT reconstructed images have a slightly higher spatial resolution than those of mART, albeit non significantly so.

6.3 Summary

It is shown from the results in the previous sections that mART produces images of superior quality to those of OctopusCT at small numbers of projections. This means that OctopusCT can be suitably replaced by mART for the reconstruction of small projection number scans.

The SART algorithm that mART implements is a flexible algorithm which can be extended into spectral reconstruction. Combining reconstruction and material decomposition produces datasets in terms of material density instead of linear attenuation, due to the same basic linear expression that they both share from Equation (6-1), and is the primary idea for mART's future extension into spectral reconstruction.

Chapter 7

Conclusion

This thesis explored how scans using the MARS spectral CT with different numbers of projections, exposure time products (mAs), and peak tube voltages (kVp) with different threshold energies (kV) affected the image noise, image resolution and image uniformity. The results from the experiments suggest that for scans using the Medipix3.0 silicon quad detector on small pre-clinical biological samples, the best balance between the image quality and radiation exposure is achieved when the scan parameters are set to the values presented in Table 7.1. These values only apply to the Medipix3.0 silicon quad detector, and not the cadmium telluride and gadolinium arsenide detectors, because those detectors were occupied most of the time and insufficient time was available to repeat the experiments on them to obtain any data; in addition, the Medipix3.1 and Medipix3.2 chips were unavailable for pre-clinical scanning at the time of the experiments. However, the general physical relationships that were observed between the scan parameters and the image quality from the experiments can be safely assumed to stand for all of these Medipix detectors. It was also concluded that the newly developed image reconstruction software mART outperforms OctopusCT in terms of the image quality, especially for small numbers of projections, which has the added benefit of minimizing radiation and reducing scan time. This allows OctopusCT to be suitably replaced by mART for the reconstruction of small projection number scans and sets the first milestone for mART's future

extension into spectral reconstruction.

Table 7.1: Optimal scan parameters for the Medipix3.0 silicon quad detector.

Scan Parameters	Optimal Settings
Number of Projections	1440
Tube Voltage (kVp)	50
Threshold Energy (kV)	15
Exposure Time Product (mAs)	0.5 at 1.68M

References

[*Sie*(2011)] Computed tomography. its history and technology, 2011.

[*Al-Nahhas A*(2007)] Al-Nahhas A, e. a., Gallium-68 pet: A new frontier in receptor cancer imaging, *Anticancer Research*, *27*, 2007.

[*AN van Daatselaar*(2004)] AN van Daatselaar, PF van der Stelt, J. W., Effect of number of projections on image quality of local ct, *Dentomaxillofacial Radiology*, 2004.

[*Andersen and Kak*(1984)] Andersen, A. H., and A. C. Kak, Simultaneousalgebraic reconstruction technique (sart): A superior implementation of the artalgorithm, *Ultrasonic Imaging*, *6*, 81–94, 1984.

[*Anderson et al.*(2010)] Anderson, N., et al., Spectroscopic (multi-energy) ct distinguishes iodine and barium contrast material in mice, *Eur Radiol*, *20*, 2126–2134, 2010.

[*Bates and Peters*(1971)] Bates, R. T. H., and T. M. Peters, Towards improvements in tomography, *N. Z. J. Sci.*, *14*, 883–896, 1971.

[*Boas and Fleischmann*(2011)] Boas, F. E., and D. Fleischmann, Evaluation of two iterative techniques for reducing metal artifacts in computed tomography, *Radiology*, 2011.

[*Budinger and Gullberg*(1974)] Budinger, T. F., and G. T. Gullberg, Three-dimensional reconstruction in nuclear medicine by iterative least- squares

and fourier transform techniques, Tech. Rep. LBL–2146, California Univ., Berkeley (USA). Lawrence Berkeley Lab., 1974.

[*CERN*(2012)] CERN, What is medipix3?, 2012.

[*Chen et al.*(2008)] Chen, G. H., J. Tang, and S. Leng, Prior image constrained compressed sensing piccs: A method to accurately reconstruct dynamic ct images from highly undersampled projection data sets, *Medical Physics*, *35*, 660–663, 2008.

[*Connolly*(2012)] Connolly, J. R., The interaction of x-rays with matter and radiation safety, *Introduction to X-Ray Powder Diffraction*, 2012.

[*Connor EE*(2005)] Connor EE, Mwamuka J, G. A. M. C. W. M., Gold nanoparticles are taken up by human cells but do not cause acute cytotoxicity, *Small*, *1*, 2005.

[*E and R*(2007)] E, R., and P. R, K-edge imaging in x-ray computed tomography using multi-bin photon counting detectors, *Phys. Med. Biol.*, *52*, 2007.

[*Fang Zheng*(2009)] Fang Zheng, Gong Hui, Y. G. Z. T., Effect of projection number on slice image quality of micro-ct system, *MIPPR*, 2009.

[*Gilbert*(1972)] Gilbert, H., Iterative methods for the three-dimensional reconstruction of an object from projections. journal of theoretical biology, *Journal of Theoretical Biology*, *36*, 105–117, 1972.

[*Gordon et al.*(1970)] Gordon, R., R. Bender, and G. Herman, Algebraic reconstruction techniques (art) for three-dimensional electron microscopy and x-ray photography., *Journal of Theoretical Biology*, *29*, 471–481, 1970.

[*Guan and Gordon*(1996)] Guan, H., and R. Gordon, Computed tomography using algebraic reconstruction techniques (arts) with different projection

access schemes: a comparison study under practical situations, *Physics Medicine and Biology*, *41*, 1727–1743, 1996.

[*Hanson*(1990)] Hanson, K. M., *Radiology of the Skull and Brain*. Mosby, 1990.

[*Hauck TS*(2008)] Hauck TS, Ghazani AA, C. W., Assessing the effect of surface chemistry on gold nanorod uptake, toxicity, and gene expression in mammalian cells, *Small*, *4*, 2008.

[*Hounsfield*(1973)] Hounsfield, G., Computerized transverse axial scanning (tomography): Part 1. description of system, *British Journal of Radiology*, *46*, 1016–1022, 1973.

[*inCT*(2012)] inCT, Octopus manual 8.2, *inCT*, 2012.

[*John A. Mayo*(1995)] John A. Mayo, Thomas E. Hartman, K. S. L. S. L. P. S. V. N. L. M., Ct of the chest: Minimal tube current required for good image quality with the least radiation dose, *AJR: 164*, 1995.

[*Kaczmarz*(1937)] Kaczmarz, S., Angenherte auflsung von systemen linearer gleichungen, *Bulletin International de l'Acadmie Polonaise des Sciences et des Lettres. Classe des Sciences Mathmatiques et Naturelles. Srie A, Sciences Mathmatiques*, *35*, 355–357, 1937.

[*Linscott*(2012)] Linscott, E., Procedures for image quality assessment, 2012.

[*McNitt-Gray*(2005)] McNitt-Gray, M. F., Tradeoffs in ct image quality and dose, *David Geffen School of Medicine at UCLA*, 2005.

[*N. G. Anderson*(2010)] N. G. Anderson, e. a., Spectroscopic (multi-energy) ct distinguishesiodine and barium contrast material in mice, *European Society of Radiology*, 2010.

[*Nanni C*(2006)] Nanni C, e. a., Role of 18f-fdg-pet and pet/ct imaging in thyroid cancer, *Biomedicine Pharmacotherapy*, *60*, 2006.

[*Nelson*(2001)] Nelson, W. R., *Interactions of 0.3 MeV photons in aluminum and lead*. National Accelerator Laboratory, 2001.

[*Ogden*(2011)] Ogden, K., Ct radiographic techniques, *UPSTATE MEDICAL UNIVERSITY radiology*, 2011.

[*R. Ballabriga*(2010)] R. Ballabriga, M. Campbell, E. H. X. L. L. T. W. W., Medipix3: A 64 k pixel detector readout chip working in single photon counting mode with improved spectrometric performance, 2010.

[*Radon*(1917)] Radon, J., ber die bestimmung von funktionen durch ihre integralwerte lngs gewisser mannigfaltigkeiten, *Akad. Wiss.*, *69*, 262–277, 1917.

[*Reddinger*(1998)] Reddinger, W., Ct image quality, 1998.

[*Riedel*(2011)] Riedel, M., An introduction to dual energy computed tomography, *University of Texas Health Science Center at San Antonio*, 2011.

[*Rusinek H*(1998)] Rusinek H, e. a., Pulmonary nodule detection: Low-dose versus conventional ct, *Radiology*, *209*, 1998.

[*Serman*(2011)] Serman, N., Production of x-rays and interactions of x-rays with matter, *Columbia University In the City of New York*, 2011.

[*Sheikh and Bovik*(2005)] Sheikh, H., and A. Bovik, Information theoretic approaces to image quality assessment, 2005.

[*Stephane Sammartino and Capowiez*(2011)] Stephane Sammartino, E. M., and Y. Capowiez, A novel method to visualize and characterize preferential flow in undisturbed soil cores by using multislice helical ct, *Vadose Zone Journal*, 2011.